Aircraft Measurements for Understanding Air-Sea Coupling and Improving Coupled Model Predictions

Djamal Khelif
Department of Mechanical and Aerospace Engineering
University of California, Irvine
Irvine, CA 92697-3975
phone: (949) 824-7437 fax: (949) 824-8585 email: dkhelif@uci.edu

Award Number: N00014-10-1-0297

LONG-TERM GOALS

The long-terms goals of our research are to understand and parameterize the physics of air-sea interaction and the Marine Atmospheric Boundary Layer (MABL) over a wide spectrum of wind speeds, sea state and cloud coverage.

OBJECTIVES

The project objective is to obtain coordinated measurements in the atmosphere, the ocean, and the air-sea interface for the purpose of coupled model evaluation and improvements. Our specific objective is to measure and map the air-sea fluxes of latent heat, sensible heat and momentum, and characterize the fine vertical structure of tropical boundary layer and map the ocean surface waves in different phases of the Madden Julian Oscillation (MJO) and over a range of scales.

APPROACH

To address the science objectives regarding air-sea interaction and tropical convection in the Indian Ocean that lead to the MJO, we participated in the LASP/DYNAMO field experiment in Nov-Dec 2011 using the NOAA WP-3D N43RF (P3) aircraft. The P3 has the range and endurance to allow the bridging of observations from other investigators on distant fixed locations on ships and islands. The unique blend of P3 PIs resulted in a unique and synergetic blend of instrumentation suites that included state and thermodynamics variables, turbulence, cloud microphysics, atmospheric radiation, SST IR imaging, ocean waves mapping, vertical-scanning Doppler radar and horizontal scanning radar, air expendables GPS windfinding dropsondes, Airborne eXpendable Bathy Thermographs (AXBT) and Airborne eXpendable Conductivity Temperature and Depth probes (AXCTD) for simultaneous atmospheric and oceanic profiling. To achieve our own specific objectives, we equipped the P3 aircraft with redundant fast-response temperature, humidity, and wind instrumentation for turbulence and fluxes measurements and with a nadir scanning lidar for ocean waves mapping as shown in Fig. 1 and listed in Table 1.

Report Documentation Page

Form Approved
OMB No. 0704-0188

1. REPORT DATE	2. REPORT TYPE	3. DATES COVERED
30 SEP 2013		**00-00-2013 to 00-00-2013**

4. TITLE AND SUBTITLE	5a. CONTRACT NUMBER
Aircraft Measurements for Understanding Air-Sea Coupling and Improving Coupled Model Predictions	5b. GRANT NUMBER
	5c. PROGRAM ELEMENT NUMBER
6. AUTHOR(S)	5d. PROJECT NUMBER
	5e. TASK NUMBER
	5f. WORK UNIT NUMBER
7. PERFORMING ORGANIZATION NAME(S) AND ADDRESS(ES) **University of California, Irvine,Department of Mechanical and Aerospace Engineering,Irvine,CA,92697-3975**	8. PERFORMING ORGANIZATION REPORT NUMBER
9. SPONSORING/MONITORING AGENCY NAME(S) AND ADDRESS(ES)	10. SPONSOR/MONITOR'S ACRONYM(S)
	11. SPONSOR/MONITOR'S REPORT NUMBER(S)

12. DISTRIBUTION/AVAILABILITY STATEMENT
Approved for public release; distribution unlimited

13. SUPPLEMENTARY NOTES

14. ABSTRACT

15. SUBJECT TERMS

16. SECURITY CLASSIFICATION OF:			17. LIMITATION OF ABSTRACT	18. NUMBER OF PAGES	19a. NAME OF RESPONSIBLE PERSON
a. REPORT **unclassified**	b. ABSTRACT **unclassified**	c. THIS PAGE **unclassified**	**Same as Report (SAR)**	**13**	

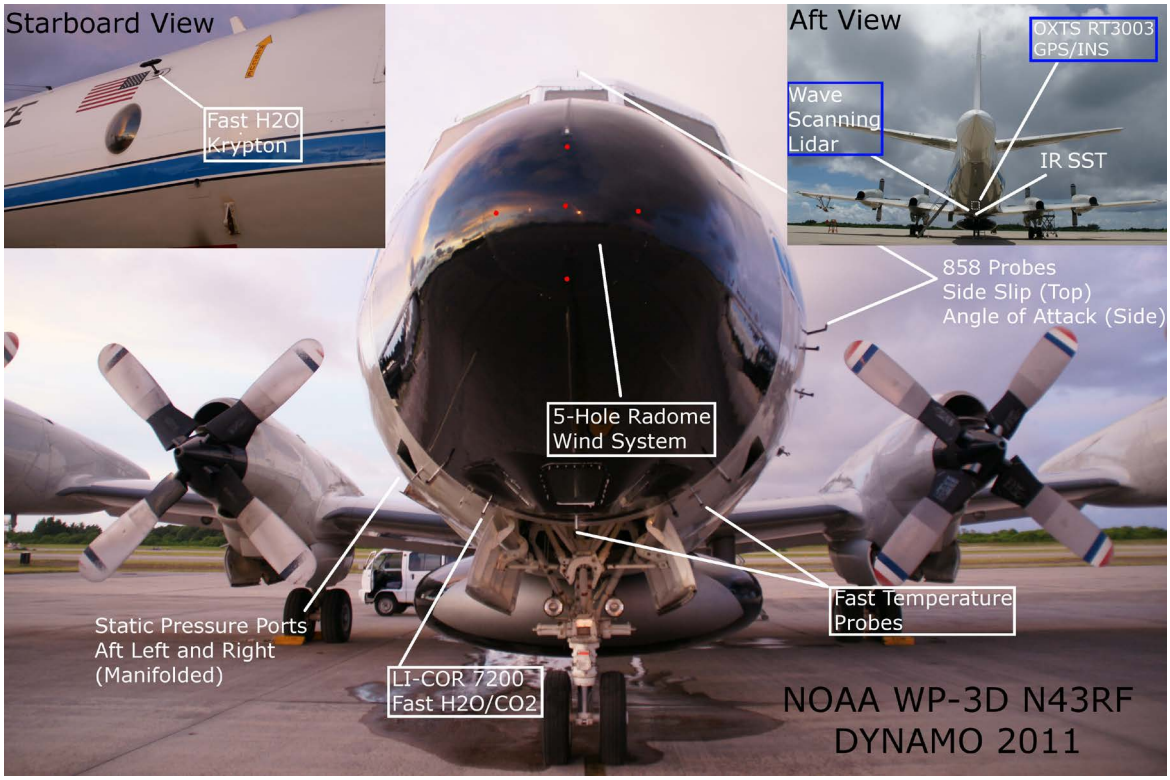

Figure 1. Turbulence and wave instrumentation installed on the NOAA WP-3D N42RF aircraft for LASP/DYNAMO 2011. (UCI-contributed instruments are identified with a box.)

Table 1. NOAA P3 Inventory of UCI-contributed instrumentation to the NOAA WP-3D N42RF and summary of their performance during LASP/DYNAMO experiment in 2011.

DYNAMO NOAA WP-3D N43RF	November 11 - December 13 2011											UTC Date
	11/11	11/13	11/16	11/19	11/22	11/24	11/26	11/28	11/30	12/04	12/08	12/13
Instrument Flight	RF 01	RF 02 *	RF 03	RF 04	RF 05	RF 06	RF 07 *	RF 08	RF 09 *	RF 10	RF 11	RF 12
Total Temperature Thermistor												
Rosemount Temperature												
LI-COR 7200 CO2												
LI-COR 7200 Humidity												
Mod. Krypton Hygrometer												
Pitch Angle Rate Sensor												
Radome Gust System												
OXTS RT3003												
OXTS Base Station												
RIEGL LMS Q240i												
Heitronics IR SST												

Legend				
UCI	Operational	Some data	No data	* NOAA DATA Gaps
NOAA AOC	Convection Mission		Boundary Layer Mission	

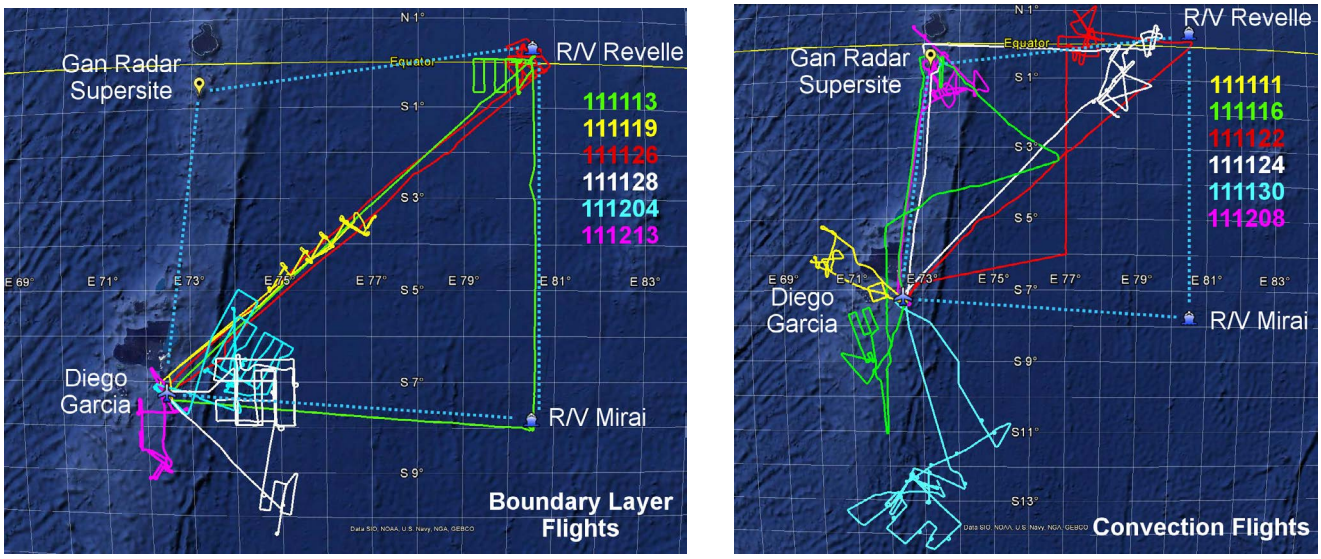

Figure 2. LASP/DYNAMO 2-D flight tracks of the NOAA WP-3D aircraft during boundary missions (top) and convection missions (bottom) where each flight is identified by its YYMMDD UTC date.

The NOAA/AOC WP-3D N43RF flew a total of 12 flights (9-10 hours each), half of which were convection-centric while the other half were boundary-layer-centric as shown in the 2-D flight tracks on Fig. 2. Most flights did include a flight pattern module or two from the other focus of the study with the aim of obtaining an as complete as possible characterization of the different processes involved. Boundary-layer flights are naturally of prime interest to our effort focus and we included in them 3 major flight modules (Fig. 2). They consist of a vertical stack of level legs for boundary layer turbulence fluxes profile sampling; a cross-section profiling module for the characterization of the vertical structure of the boundary layer, and a flux mapping module at about 60 m above the ocean surface to characterize the horizontal variability of the surface fluxes.

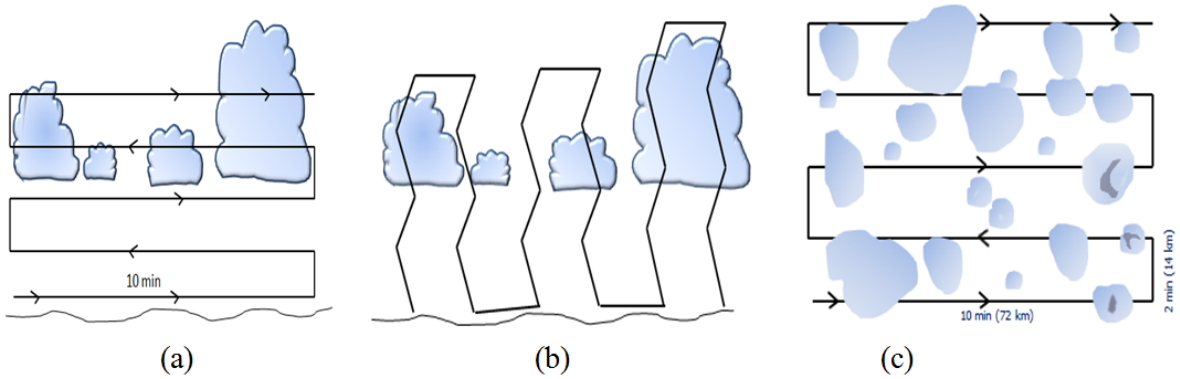

Figure 3. Boundary layer flight modules: (a) vertical stack (side view), (b) cross-section profiling (side view) and (c) surface flux mapping (top view).

WORK COMPLETED

Data quality control was systematically performed on data from all instruments we contributed and on data from other instruments that are required for our research effort. Overall, the instruments performed well during the field experiment as summarized in Table 1. Redundancy in measurement systems was instrumental in insuring that no critical data were lost. However, due to the first implementation of a new data system that NOAA/AOC finished developing days before the field experiment, there were some occasional hiccups. These were in the form of dropouts in the fast-rate (50-Hz and 25-Hz) data on all flights (identified by green vertical lines in the typical example shown in Fig. 4) as well as some data gaps that occurred on 3 flights (identified by an asterisk on Table 1) when the data system malfunctioned and had to be restarted by the operator. Using 100–Hz data from our independent measurements (OXTS INS/GPS 100-Hz unit), we developed a technique to fix these dropouts and gaps and to synchronize the data from the different systems without which it would have been nearly impossible to process the high-rate data.

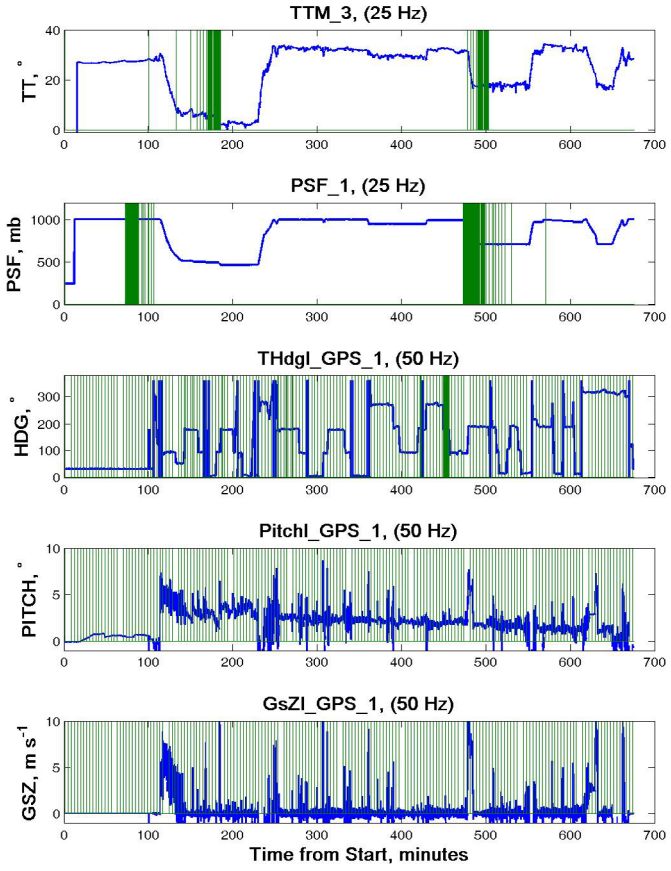

Figure 4. Typical example of raw fast-rate (25 Hz and 50 Hz) data recorded by the new NOAA/AOC data system. The select variables shown are (from to bottom): total temperature, static pressure, aircraft heading angle, pitch angle and grounds speed. The green vertical lines are markers for data dropouts that required to be fixed before further processing.

NOAA/AOC processes only 1-Hz data and provides standard 1-Hz flight data but these are not suitable for eddy correlation and turbulence statistics calculations. The fast-rate data are recorded at either 25-Hz (analog signals) or 50-Hz (INS/GPS, radar altimetry etc…) and required processing. A significant part of our effort was dedicated to developing software to reduce and process the high-rate data into high-bandwidth winds, humidity, temperature etc. so that turbulence statistics and fluxes can be computed. The fuselage and radome vertical wind components were calibrated and checked using pitching maneuvers data (see example in Fig. 4). These maneuvers were specifically flown for this purpose in quiescent air well above the boundary layer where any variability in the vertical wind is assumed artificially induced by the aircraft pitching motion. Thus, the ratio of the standard deviation of the vertical wind to that of the aircraft vertical velocity should be minimal. It was found to be 3% and 4% for the UCI-calculated fuselage (WZF, red) and radome (WZR, green) vertical winds, respectively, and 11% and 18% for UWZ and WSZ, respectively, the two NOAA/AOC vertical wind variables that are available in the 1-Hz standard data files. The vertical wind passes the test when this ratio is less than 10% according to a commonly accepted rule of thumb. This is a very important step as the vertical wind is the most critical measurement for fluxes calculation.

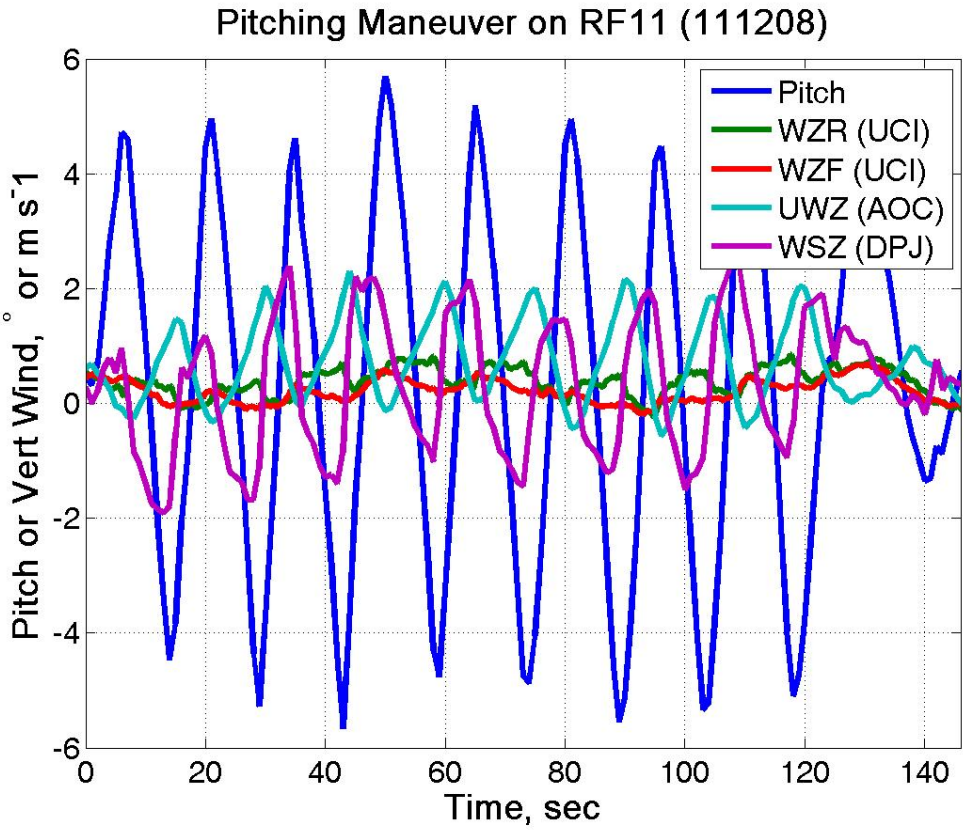

Figure 4. Aircraft pitching maneuver performed in quiescent air above the boundary layer to check and calibrate the vertical wind. Any variability in the vertical wind is artificially induced by the aircraft pitching motion. The ratio of the standard deviation of the vertical wind to that of the aircraft vertical velocity was found to be 3% and 4% for the UCI-calculated fuselage (WZF, red) and radome (WZR, green) vertical winds, respectively, and 11% and 18% for UWZ and WSZ, respectively, the two NOAA/AOC vertical wind variables that are available in the 1-Hz standard data files. The vertical wind passes the test when this ratio is less than 10% according to a commonly accepted rule of thumb.

An example UCI-processed winds from both the radome and the fuselage gust systems are shown in Fig 5. Winds from the two systems are in very good agreement except for the vertical component at ~6000 m altitude due to icing of the angle of attack pressure port on the radome system. (This is not a concern since we do not expect to measure turbulence at that high altitude). The LI-COR 7200 and Krypton fast humidity data were calibrated against flight data from slow-response chilled mirror. Details on the wind and humidity calibration techniques can be found in Khelif et al. (1999).

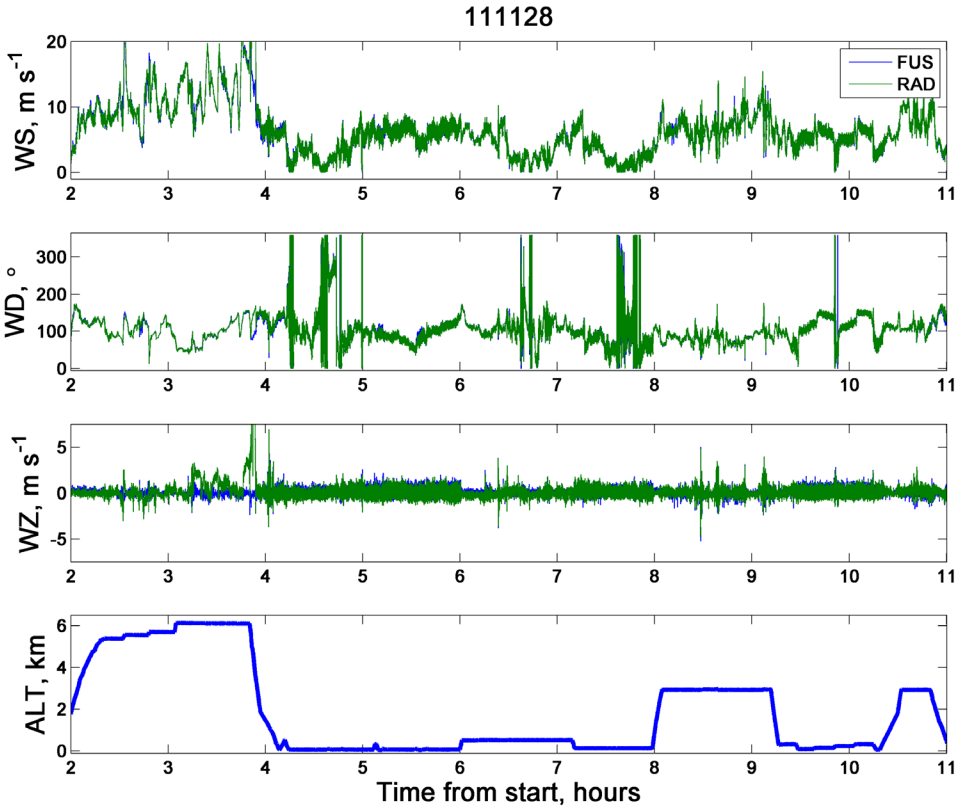

Figure 5. Time series (25-Hz) of UCI-processed wind from the radome (green) and the fuselage (blue) gust systems of (from top) the wind speed, wind direction and wind vertical component. The pressure altitude is plotted in the bottom panel. Winds from the two systems are in very good agreement except for the vertical component at ~6000 m altitude due to icing of the angle of attack pressure port on the radome system. (This is not a concern since we did not expect to measure turbulence at that high altitude). Data are from RF08 from Nov 28, 2011.

So far 3 processing iterations were performed on data from all 12 flights. A data set that includes all P3 aircraft soundings with a 25-Hz sampling rate and its descriptive "readme" file are available on our data server at this URL: http://wave.eng.uci.edu/files/DYNAMO/data/UCI_P3Soundings_25Hz/ .

Similarly, the 50-Hz navigation and attitude data set from our OXTS RT3003 INS/GPS that include real-time OmniStar correction and post-flight differential GPS correction and its descriptive "readme" file are available on our data server at this URL:
http://wave.eng.uci.edu/files/DYNAMO/data/UCI_OXTS_RT3003_INS-GPS_50Hz_CSV/

The DYNAMO data sets archive hosted at NCAR/EOL provides links to both of these data sets.

RESULTS

In this section we present preliminary analysis as most of our effort concentrated on the data processing that required more time as explained in the previous section. Eddy Correlation fluxes and mean variables were calculated from 3-minutes (corresponding to ~18 km) contiguous segments "cut" on all level and straight runs. The ogive method was used to determine the flux estimates as the low-frequencies asymptote value on the cumulative integral (integration done from high to low frequencies) of the cross-spectrum between the vertical wind and the relevant variable. Results from 188 lowest levels (~60 m or less) segments are shown on Fig. 6 (means) and Fig. 7 (fluxes) for all flights except for the Dec 8, 2011 flight during which no flux runs were carried out since it was totally dedicated to convection work. Each green dot on those plots represents data from one segment and the blue line represents the averages from all segments on the given flight. In general, the variability and trend of the fluxes reflect those of the means of the variables they are associated with.

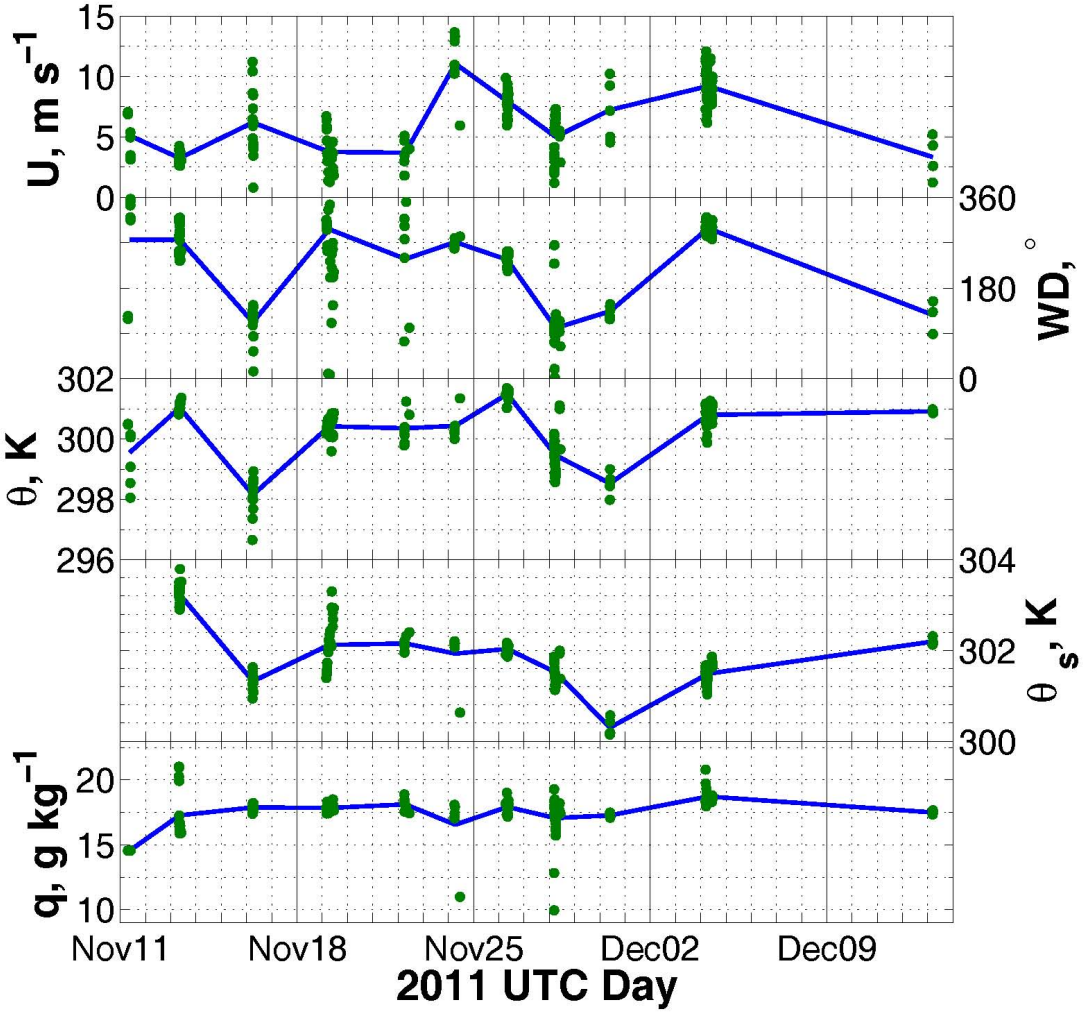

Figure 6. Mean variables obtained from 188 3-minute segments (~ 20 km) from straight and level runs at $z \leq 60$ m. Each green dot represents the average from one such segment and the blue line the flight average of (from to bottom) wind speed, wind direction, air potential temperature, radiometric sea surface temperature and specific humidity.

The onset of the MJO on Nov 24 is characterized by a veering wind to the west 4 days prior and with a sudden increase in wind speed from 3 m s^{-1} to over 11 m s^{-1}. This was accompanied by a dramatic increase of the total stress from less than 0.05 Pa to over 0.15 Pa and of the latent heat flux from ~50 W m-2 to ~200 W m^{-2}. It is quiet remarkable that the air-sea temperature difference drops fairly quickly after the onset of the MJO. The air-sea temperature difference decreased relatively quickly after the event. This confirms findings by Qing Wang from an analysis using lower levels of drop sounds data and upper levels of Abets data. Similar but less dramatic changes are also observed on the milder second MJO that peaked on Dec 4.

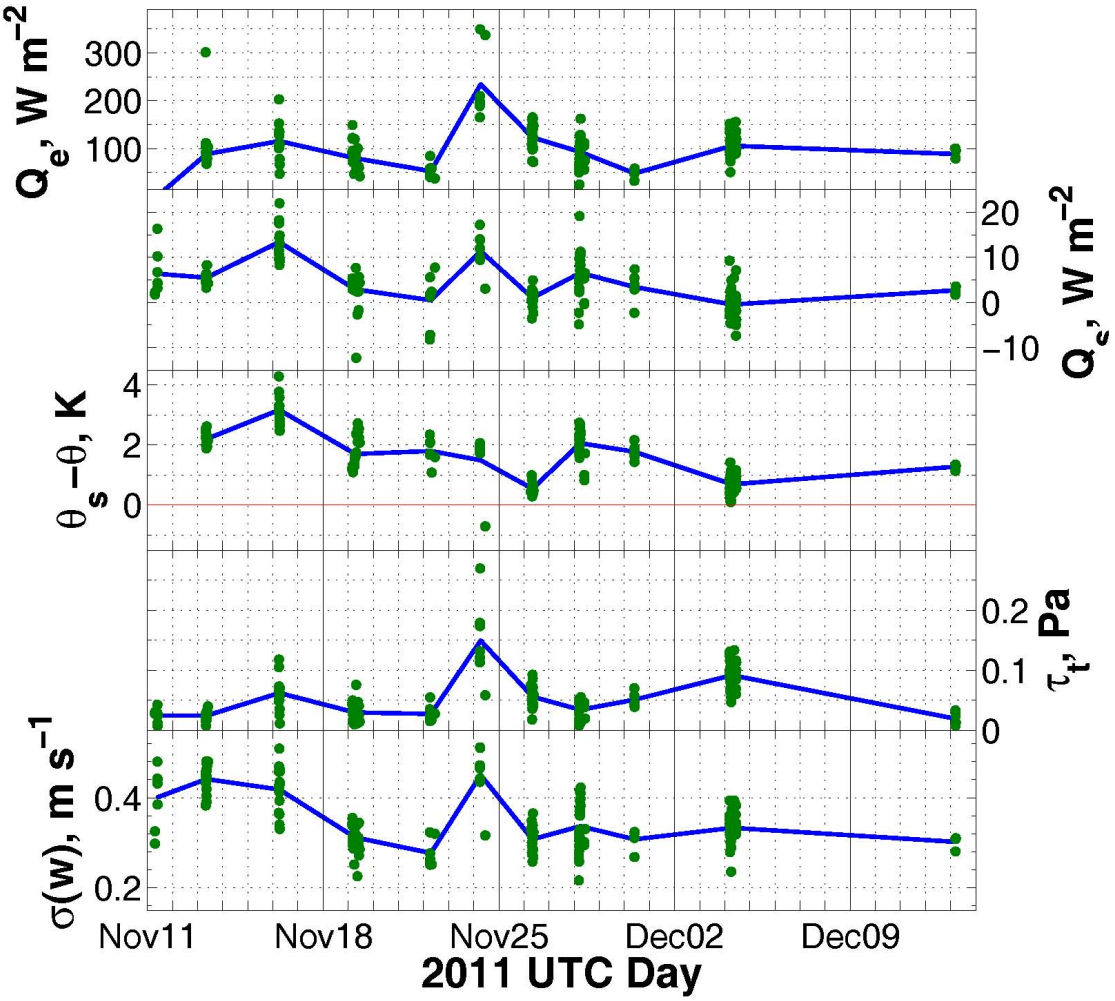

Figure 7. Eddy correlation fluxes obtained from 188 3-minute segments (~ 20 km) from straight and level runs at z ≤ 60 m. Each green dot represents the estimate from one such segment and the blue line the flight average of (from to bottom) , latent heat flux, sensible heat flux, sea surface-air potential temperatures difference, total stress and standard deviation of vertical wind.

Within an individual run the variability of the latent heat flux was explored by examining the time series of the latent heat obtained with the running averaging technique using 180-s sliding (~20 km) window. As shown in Fig. 8, the flux responds to mesoscale variability in the absolute humidity (run

from Nov 13) and both in the absolute humidity and vertical wind components (run from Nov 26). We are exploring ways to determining flux contributions from different scales in different phases of the MJO by using this technique with different window sizes.

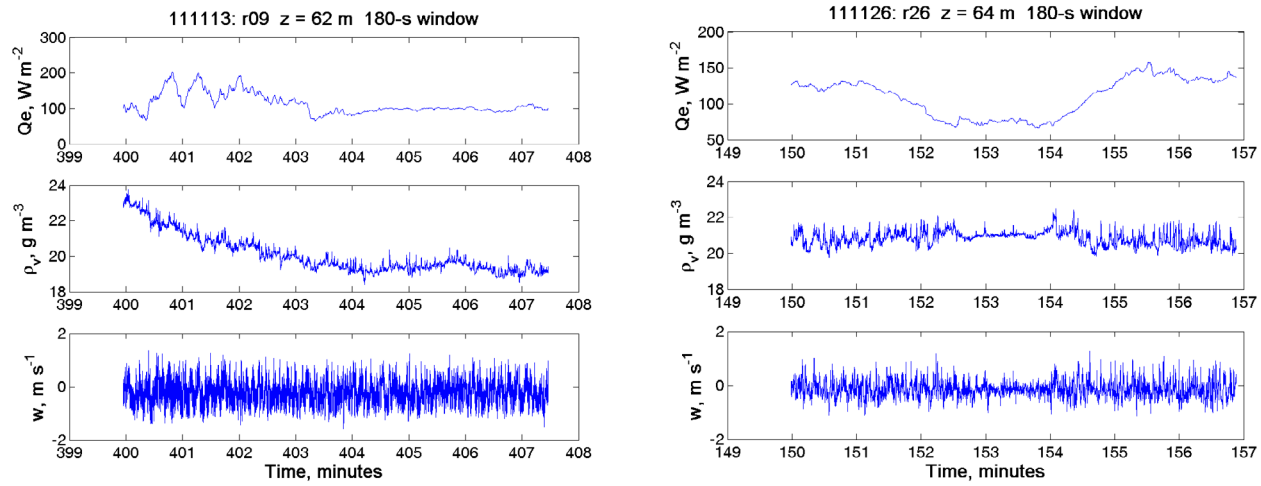

Figure 8 Variability of eddy correlation latent heat flux (top) on individual 60-m runs on Nov 11 (left) and Nov 26 (right) 2011. A running averaging technique with a sliding window of 180 s (~20 km) was used for the flux estimates. Absolute humidity and wind vertical component are plotted in the middle and bottom panels, respectively.

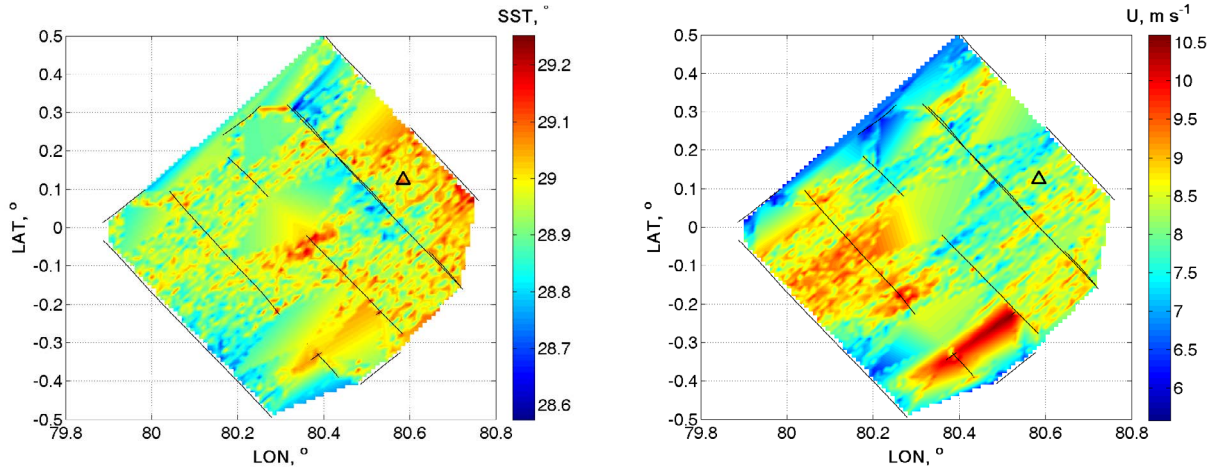

Figure 9. Contour maps of radiometric SST (left) and wind speed (right) obtained from ~ 60-m P3 runs (black lines) in the vicinity of the R/V Revelle (Δ) on Nov 26, 2011.

A sample of SST and wind speed mapping in the vicinity of the R/V Revelle on Nov 26, 2011 is shown in Fig. 9. Although the contouring may need some refining, these maps seem to reveal the horizontal variability as identified by the structure in both parameters.

Mean wind speed, specific humidity, SST and turbulent fluxes of momentum (stress), latent heat and sensible heat from 180-s averages (~20 km) on runs at ~ 60 m near the R/V Revelle on Nov 13

(suppressed MJO phase) and on Nov 26 (two days after the Thanksgiving main MJO event) are compared with their ship counterparts in Fig. 10. Although these runs are not direct overpasses, the agreement between the aircraft and the ship measurements is reasonable and within the spatial and temporal variability of the quantities that are compared. The only exception is the mean humidity from the aircraft on Nov 13 that will require further scrutiny.

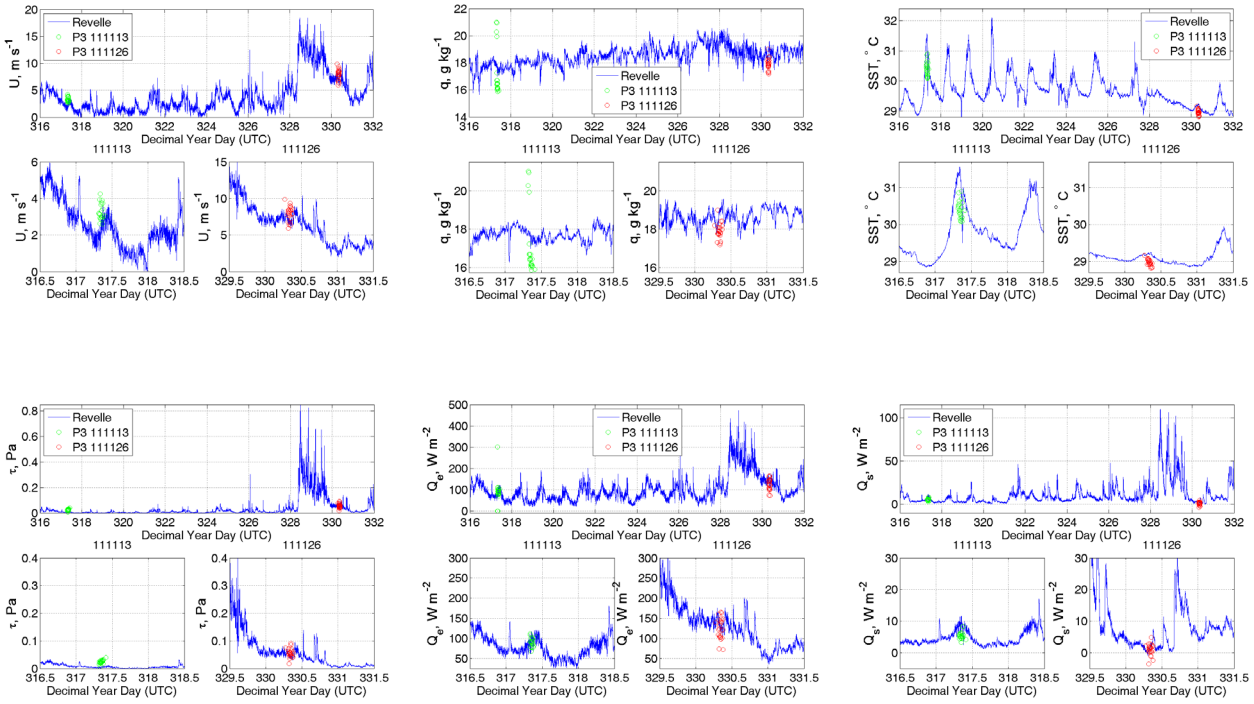

Figure 10. Comparisons between P3 (Nov 13, green circles and Nov 26 red circles) and R/V Revelle (blue lines) of (from right to left and top to bottom) wind speed, specific humidity, SST, stress, latent heat flux and sensible heat flux. For each parameter an overall plot is shown on top and two plots below it show 2 days only of the ship data to convey the variability in the measurements.

We put together a wave mapping system (Fig 11a) essentially consisting of a scanning eye-safe lidar and a collocated highly accurate INS/GPS unit (Oxford RT3003) that uses real-time correction from OmniStar positioning service and post-flight correction from a dedicated differential GPS base station we set up by the airport. The whole system was calibrated using the boresighting technique just after return from LASP/DYNAMO experiment on a dedicated flight with a grid pattern over a residential area with pitched roofs buildings in the Tampa Bay area (Fig.11b). Data from such a pattern are processed using an optimization technique that matches and reconstitute the topography from the different scans of the grid pattern (Fig. 11c) and especially the cross section of the pitched roofs.

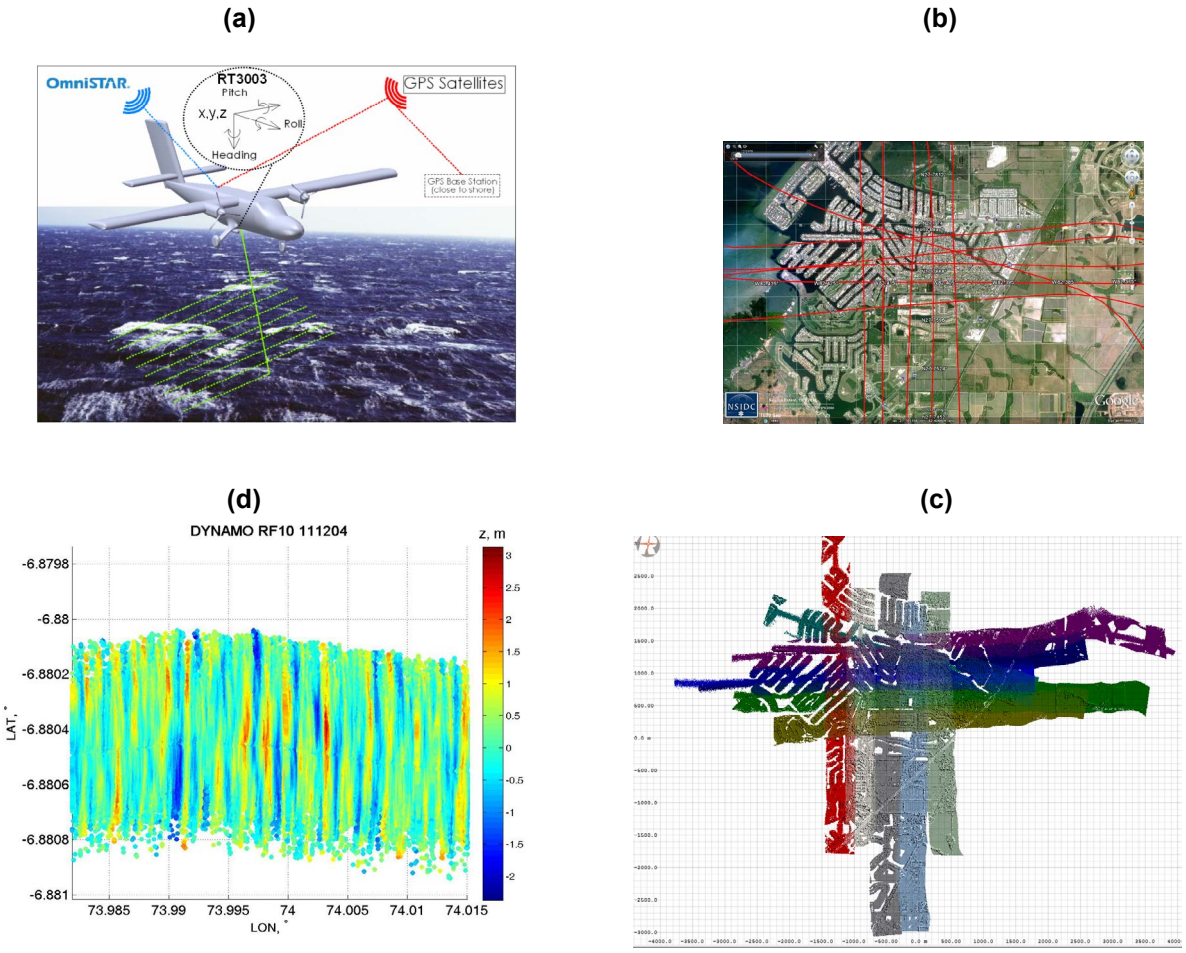

Figure 11. (a) Wave mapping system using and eye-safe lidar and a collocated highly accurate INS/GPS unit (Oxford RT3003) that uses real-time correction from OmniStar positioning service and dedicated differential GPS base; (b) grid pattern of boresighting calibration flight on 13 January, 2012 over a residential area near Tampa, FL upon return from the field experiment; (d) topography of the surveyed site as measured on each scan; (d) sample wave field topography from a LASP/DYNAMO run on December 4, 2011.

A sample result of the topography of the wave field is shown for DYNAMO flight of Dec 4, 2011. These maps are then gridded so that wave statistics and spectra can be computed using data from "digital" scans along the track and at different locations across the swath. Some sample results are shown on Fig. 12 for a suppressed phase (13Nov11), the MJO onset day (24Nov11) and the mild MJO event (04Dec11). The 4-σ significant height was 1 m, 2.6 m and 1.8 m respectively for the 3 cases shown. The most energetic waves were the shortest during the mild MJO event and the longest during the suppressed phase which is consistent with mild swell observed during that period of the experiment.

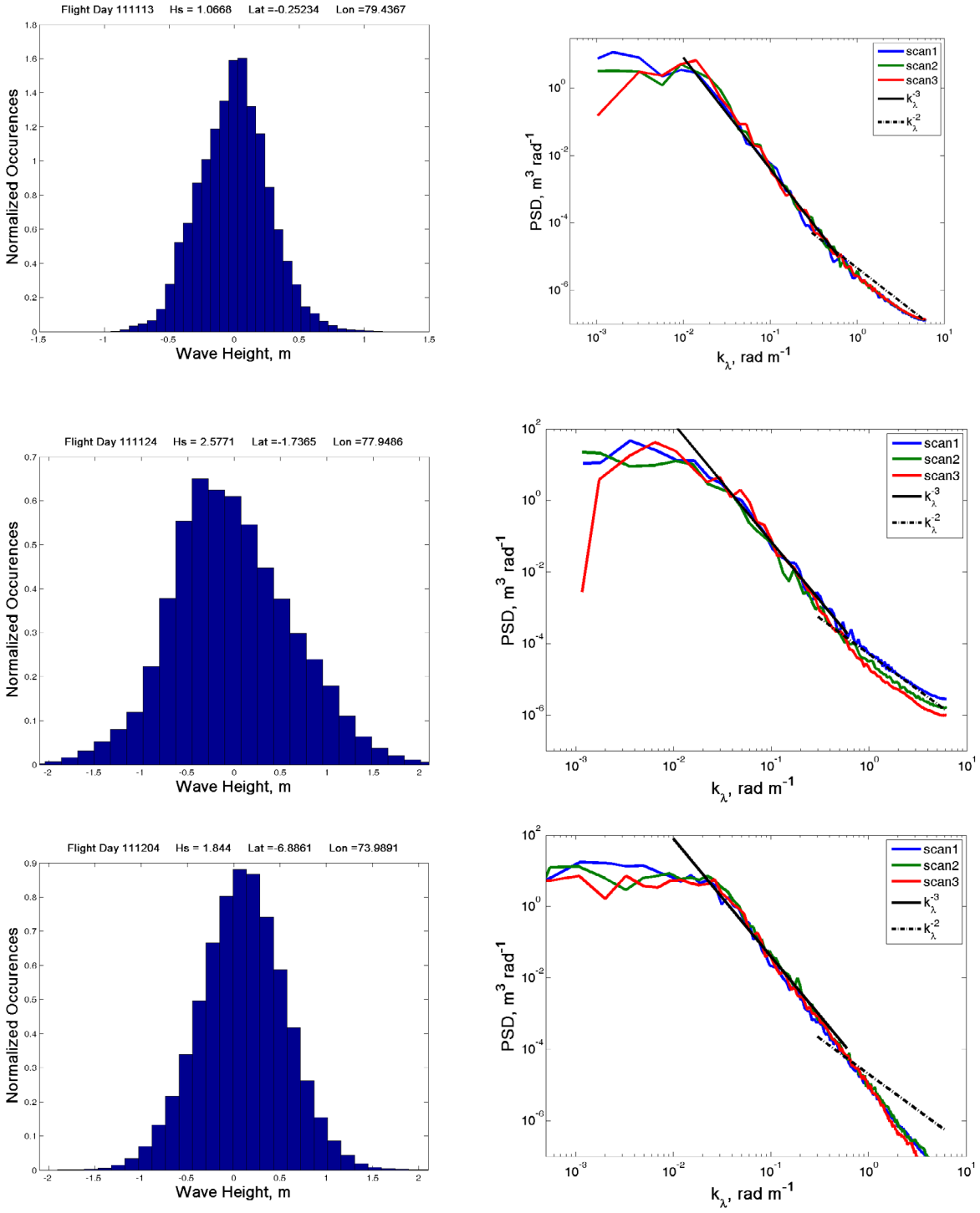

Figure 12. Wave height histograms (left) and spectra (right) on an MJO suppressed day (13Nov2011, top), an MJO active day (24Nov2011, middle) and a mild MJO event (04Dec2011). The 4-σ significant height was 1 m, 2.6 m and 1.8 m respectively for the 3 cases shown.

IMPACT/APPLICATIONS

The use of the LI-COR 7200 with our modified Rosemount total temperature probe housing used as inlet was successful. It provided reliable and fast response humidity measurements. Our modified krypton hygrometer is a good alternative to the obsolete AIR Lyman-alpha for fast-response humidity measurements from research aircraft.

TRANSITIONS

Our modification of the NOAA/AOC WP-3D radome wind system effectively prevented ingested water during in-cloud flights or through precipitation events from obstructing the pressure lines between the pressure ports and the sensing transducer. This improvement has made the radome gust system unaffected by liquid water during the hurricane survey flights which are the primary mission of the NOAA WP-3D N43RF. The same technique can be implemented to the sister aircraft N42RF.

Also NOAA/AOC has been closely cooperating with to evaluate their altimeters measurements using our high end OXTS GPS/INS measurements.

RELATED PROJECTS

None

REFERENCES

Khelif, D., S. P. Burns and C. A. Friehe, 1999: Improved Wind Measurements on Research Aircraft. J. Atmos. Oceanic Technol., 16, No. 7, 860-875.